

High Temperature X-ray Absorption Spectroscopy of the Local Electronic Structure and Oxide Vacancy Formation in the $\text{Sr}_2\text{Fe}_{1.5}\text{Mo}_{0.5}\text{O}_{6-\delta}$ Solid Oxide Fuel Cell Anode Catalyst

Andrew C. D’Orazio,[†] Tim Marshall,[†] Tamanna Sultana,[†] Janelle K. Gerardi,[†] Carlo U. Segre,[‡] Jeremy P. Carlo,[§] and Bryan C. Eigenbrodt^{*†}

[†]Department of Chemistry, Villanova University, 800 E. Lancaster Avenue, Villanova, Pennsylvania 19085, United States

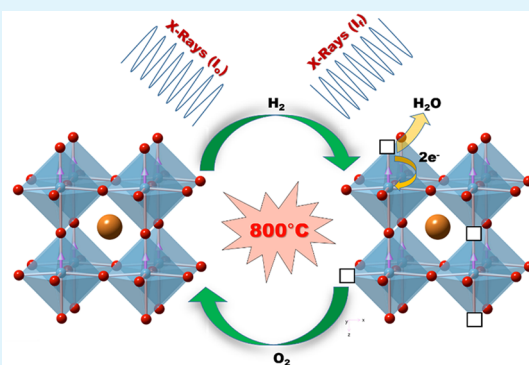
[‡]Department of Physics and CSRRI, Illinois Institute of Technology, Chicago, Illinois 60616, United States

[§]Department of Physics, Villanova University, Villanova, Pennsylvania 19085, United States

Supporting Information

ABSTRACT: Perovskite based catalysts have recently been investigated as replacements for traditional solid oxide fuel cell (SOFC) anode materials to tolerate carbon containing fuels in these devices and resist graphite formations that can lead to device failure. The use of X-ray absorption spectroscopy with a custom built reactor assembly will allow for the noninvasive exploration of the redox chemistry of the perovskite anode catalyst $\text{Sr}_2\text{Fe}_{1.5}\text{Mo}_{0.5}\text{O}_{6-\delta}$ (SFMO) when exposed to SOFC device operational conditions at a temperature of 800 °C. Specifically, XANES and EXAFS studies of the Fe and Mo K-edges were used to understand the local electronic structure and oxygen vacancy formation of these metals in SFMO under reducing and oxidizing atmospheres. While there was minimal change in the oxidation state of the Fe atom in SFMO, as observed with XANES, there were significant oxygen vacancies formed around this metal as seen with EXAFS modeling. Interestingly, the opposite was true for Mo where there was a significant change in the oxidation state of the Mo atom with marginal changes to the oxygen environment surrounding this metal. The findings from these experiments will provide an understanding of the roles that the Fe and Mo atoms play in the ionic and electronic conducting properties of this material under standard SOFC operating device conditions. More importantly, this work will provide a unique perspective into SFMO’s ability to act as an effective anode catalyst in SOFCs.

KEYWORDS: X-ray absorption spectroscopy, solid oxide fuel cells, perovskite, XANES, EXAFS



INTRODUCTION

Currently, our world relies almost completely on fossil fuels, a resource whose supply is being depleted while negatively affecting our environment. For these reasons, finding alternative energy technologies that utilize renewable resources efficiently while producing minimal pollution is of great global importance. Of the available alternative energy technologies, solid oxide fuel cells (SOFCs) have attracted considerable attention because of their ability to provide electricity with fuel efficiencies as great as 80% from a variety of different fuels (H_2 , CO , CH_4 , CH_3OH , $\text{C}_2\text{H}_5\text{OH}$, etc.).^{1–5} However, current Ni-based SOFC anodes can only operate directly with hydrogen as a fuel source to provide consistent power generation and show signs of degradation with prolonged exposure of hydrocarbon fuels.^{1,4–9} These limitations of SOFC technology have spurred the investigation of new mixed ionic and electronic conducting (MIEC) metal oxide anode catalyst materials that can be effective at generating electricity while also oxidizing away carbon deposits before they become detrimental to device performance.^{10–12}

Previous work conducted by the authors utilized a direct correlation of voltammetry with in operando Raman spectroscopy to exhibit that the perovskite anode, $\text{Sr}_2\text{Fe}_{1.5}\text{Mo}_{0.5}\text{O}_{6-\delta}$ (SFMO), is capable of operating with alcohol fuels while completely resisting detrimental graphite deposits.¹³ A key finding of this work is that SFMO was capable of operating with ethanol, which is known to form significant graphite deposits throughout the anode during device operation which are brought upon by C_2 fuel pyrolysis products.¹³ In the present work, SFMO will be explored to understand the roles that the Fe and Mo atoms, in this crystal structure, play in fuel oxidation mechanisms and afford this material its fuel tolerance capabilities seen in this previous work. Specifically, X-ray absorption spectroscopy (XAS) will be conducted at SOFC operational temperatures (800 °C) and in reactive atmospheres to investigate changes in the Fe and Mo local electronic

Received: September 17, 2018

Accepted: March 5, 2019

Published: March 5, 2019

structure and their ability to form oxygen vacancies to induce oxide ionic conduction to encourage oxidation reaction of graphite.

A SOFC device assembly consists of three principal components: a solid oxide electrolyte and two electrodes (an anode and a cathode).^{1,2,13,14} In the most general sense, the overall chemistry occurring in SOFCs converts a fuel into products and electricity in the presence of oxide anions.^{1,3,13,15,16} When hydrogen is the fuel, the sole product is H₂O. When hydrocarbon fuels are utilized, the products become a mixture of CO₂ and H₂O. A schematic of a SOFC device can be seen in Figure 1.¹³ To provide both the

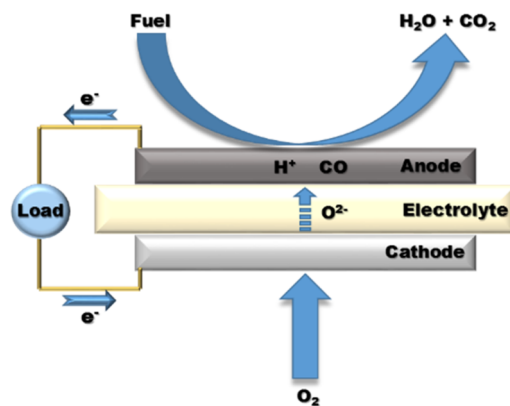


Figure 1. Schematic of the SOFC device along with general reactions for hydrocarbon fuels. Reproduced with permission from ref 13. Copyright 2018 John Wiley and Sons.

electronic and ionic conduction needed in SOFC anodes, the traditional anode material is a composite electrocatalyst consisting of a nickel (Ni) phase and 8% yttria-stabilized zirconium (YSZ) phase, also known as ceramic-metallic (cermet) composite.^{2,13,15,17,18} Ni is chosen for these anodes for its superior fuel cracking capabilities and electron conduction, while the oxygen vacancies provided through YSZ allow for oxide anion conduction.^{1,4,13,19,20}

Recent efforts to commercialize SOFC technology have moved away from hydrogen fuel due to high generation costs and challenges associated with fuel storage.^{13,21,22} Instead, SOFC development has focused on discovering and exploiting new electrocatalytic materials capable of efficiently converting hydrocarbon fuels and fuel mixtures into electricity and products.^{13,23–26} Understanding the fundamental catalytic oxidation chemistry of hydrocarbon fuels in these devices will prove to be significant because of their abundant supply in nature in the form of natural gas (methane) and their ability to be derived from renewable biological processes like bioethanol.^{27–29} This latter concept is significant, because coupling the renewable aspect of hydrocarbon fuels with the SOFC's high fuel efficiencies can lead to a potentially near carbon-neutral source of energy.

One challenge of operating SOFCs with hydrocarbon fuels is the tendency of these fuels to undergo gas phase pyrolysis and form species known to promote carbon accumulation.^{13,28,30} These graphite deposits will decrease electrode porosity and, even worse, block catalytically active Ni sites.^{1,4–10} The high sulfur content of hydrocarbon fuels, such as natural gas, also permits the reaction of H₂S with Ni to form NiS.^{10–12,31,32} The formation of NiS will also block catalytic sites, and with its low melting temperature (797 °C), agglomeration will eventually

occur in the anode microstructure.^{8–10,31,32} Specifically, with traditional Ni/YSZ anodes, fuel oxidation processes occur at the boundaries where Ni and YSZ particles meet. This requirement constrains electrochemical oxidation to reactive three phase boundaries (TPBs) where catalytically active materials, ionically conductive materials, and the gas phase fuel all meet, Figure 2a.¹³ The inability to provide oxide ions to Ni

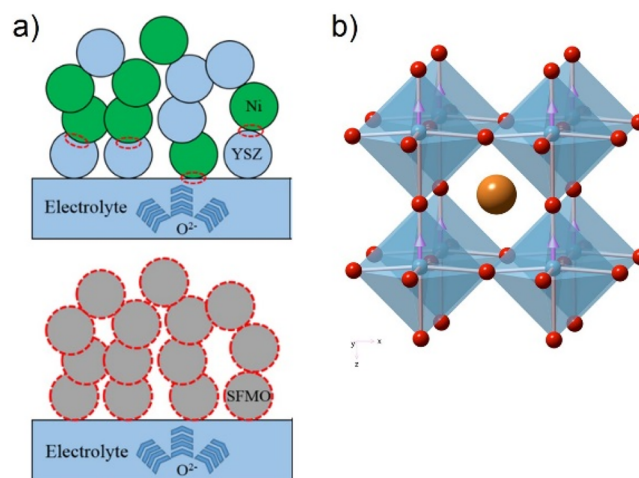


Figure 2. (a) Schematic representation of a two phase cermet anode (top) and a single phase mixed ionic and electronic conducting anode (bottom).¹³ The reactive areas are highlighted with a red dashed line. (b) 3-D crystal structure representation of the SFMO anode catalyst generated from GSAS software using the diffraction pattern. Reproduced with permission from ref 13. Copyright 2018 John Wiley and Sons.

catalytic sites located away from TPBs renders these catalysts vulnerable to poisoning from graphite and sulfur formation.^{5,13} This breakdown of the anode microstructure will negatively impact anode porosity, catalytic surface area, fuel tortuosity, and overall connectivity of the conducting Ni network also leading to device degradation and eventual failure of the device with prolonged exposure to the fuel.^{8–10,31,32}

Due to the limitations of hydrocarbon fuels in these devices, some current research efforts in this field have been in exploring the use of mixed ionic and electronic conducting (MIEC) metal oxide anode materials that have the potential to be effective at blocking carbon deposits and sulfur formations while still maintaining electrocatalytic activity or electronic conductivity.^{8–10,31,32} Since SFMO is a MIEC material, only one anode phase is needed unlike the traditional dual phase Ni/YSZ anode material. In theory, this situation will result in the entire SFMO surface being catalytically active, increasing electrochemical reactivity (Figure 2a).¹³ Specifically, this will provide sufficient oxide conduction which will enable resistance to carbon deposition and metal sulfide formations by promoting the oxidation reactions with incident fuel fragments to form CO, CO₂, SO, and SO₂.

Of the MIEC materials that have been investigated as promising candidates for SOFC anodes, those adopting a perovskite structure have shown the greatest potential for having long-term stability under standard SOFC operating conditions.^{10–13} Perovskites have an ABO₃ composition where "A" represents a 12-fold coordinated alkaline earth or lanthanide metal and "B" represents a 6-fold coordinated alkaline earth metal or a transition metal.^{10–13,31,32} Some

benefits of perovskite materials are that they can accommodate oxygen vacancies and can have limited stoichiometric variation in the crystal structure while still maintaining overall structural stability.^{10–13,31,32} These abilities allow for tunable perovskite properties that enhance catalytic activity by inducing either n-type or p-type conductivity with the addition of various dopants into the “A” sites and “B” sites of the crystal system.^{10–13,31,32} Furthermore, with the addition of dopants on the B-site, perovskites can take on the configuration of $A_2B'_{1-x}B''_xO_{6-\delta}$ to represent all possible sites for “B” metal atoms in the unit cell.^{10–13,31,32} The double perovskite of interest in these studies is $Sr_2Fe_{1.5}Mo_{0.5}O_{6-\delta}$, where Fe and Mo are introduced as the two B-site metals in this material. A representation of the perovskite crystal structure associated with SFMO is seen in Figure 2b.¹³ This research will explore the Fe and Mo metals in the “B” site of this material in an attempt to understand the roles they play in fuel tolerance, electronic and ionic conducting, and the formation of oxygen vacancies.

SFMO has many of the properties desirable in high temperature solid state electrodes. First, SFMO is stable in both oxidizing and reducing environments.^{13,33,34} Redox stability is an important quality to have as an anode material because in a SOFC device these materials are exposed to a constant reducing fuel atmosphere as well as to a constant oxide flux across the electrode–electrolyte interface.¹³ This redox stable quality has allowed SFMO to be integrated into symmetric SOFCs where it serves as both the anode and cathode.^{13,33} In regard to fuel stability, SFMO has already been shown to be an efficient anode catalyst for synthetic natural gas made of CH₄ with H₂S added as a contaminant.^{13,35,36} Another important feature of this material is that it has two “B” site centers where both Fe and Mo have the potential to assume different oxidation states, in reducing atmospheres, to provide electron conduction through varying the conduction band of the material.^{13,35,36} Other researchers have observed that Fe can assume a variety of different oxidation states (+2, +3, and +4) and the percentages of the contribution of these oxidation states will vary depending on what conditions the sample is exposed to.^{34,37–50} The same can be seen for Mo where this atom can assume a variety of different percentages of different oxidation states (+4, +5, and +6).^{34,37–50} In addition to a variety of “B” site metal oxidation states, there is also the possibility to induce the formation of oxygen vacancies, around the “B” site metals, that allow for oxide ion migration through the material to increase its resilience to carbon accumulation.

Due to the challenges of studying SOFC in operando, there is minimal understanding about the fundamental chemistry of this material that would lend to its catalytic and fuel tolerance properties. Most of the current challenges associated with SOFC research are related to the operational conditions and design of the devices themselves.^{2,51–53} These devices are fully insulated to provide the high operating temperatures (>600 °C); this results in experimentally inaccessible device architectures that make it extremely difficult to validate proposed kinetic models because of lingering questions about elementary reactions occurring in the SOFC during operation.⁵¹ Because of these challenges, research efforts regarding these devices are limited to the correlation between electroanalytical and ex situ characterization measurements.^{51,54–56} Since these ex situ measurements are conducted after the device has been brought to room temperature and disassembled, they cannot provide a direct correlation between

electrochemical performance with specific chemical and materials changes occurring in the SOFC during operation. In an attempt to understand the fundamental chemistry occurring in the extreme environments of SOFCs, first-principles computational methods like those conducted by Munoz-Garcia et al. are typically used. Specifically, Munoz-Garcia et al. was one of the first groups to try and understand the fundamental chemistry of the SFMO material by performing DFT+U computational studies to gain insight in the sources of oxygen vacancy formations and electronic conduction in this material.³⁴ Recently, researchers have been finding ways to experimentally explore these devices in operando or under these extreme operating conditions.^{5,8,30,57–60} Having the ability to conduct measurements under standard operational conditions can provide essential insight into SOFC chemistry that could not normally be obtained from standard ex situ or electrochemical measurements and can also help to verify existing computational models.¹³

The research conducted in this paper utilized a custom-built XAS chamber to permit for the high temperature (800 °C) XAS measurements of the SFMO catalyst while being exposed to reducing and oxidizing conditions. The purpose of these measurements will be to explore and understand how the Fe and Mo metals in this material participate in the electronic and ionic conducting properties of SFMO and how this can lend to its fuel tolerance capabilities. Specifically, an in-depth analysis of the X-ray absorption near edge structure (XANES) and extended X-ray absorption fine structure (EXAFS) portions of the XAS spectrum for the Fe and Mo K-edges will be conducted. The data gained from these measurements will provide information about changes in metal oxidation state that can aid in electron conduction and locate the presence of oxygen vacancy formations which can induce ionic conduction in these materials.

■ EXPERIMENTAL SECTION

Sr₂Fe_{1.5}Mo_{0.5}O_{6-δ} Synthesis. The Sr₂Fe_{1.5}Mo_{0.5}O_{6-δ} (SFMO) anode material was prepared via a solution–gel (sol–gel) synthesis technique.¹³ In this sol–gel synthesis, separate metal-ion stock solutions were created and calibrated for Fe(NO₃)₃·9H₂O and (NH₄)₆Mo₇O₂₄·4H₂O (Alfa Aesar). Stoichiometric amounts of the iron and molybdenum stock solution along with anhydrous Sr(NO₃)₂ (Alfa Aesar) were introduced into a reaction flask with a (Sr²⁺:Fe³⁺:Mo⁶⁺) molar ratio of 2:1.5:0.5.¹³ This mixed metal ion solution was allowed to mix for 30 min at room temperature, while the chelating agent, EDTA, was measured separately to have a metal ion to EDTA molar ratio of 1:1.5.¹³ The EDTA was then fully dissolved in NH₄OH (Sigma-Aldrich) before it was added slowly to the mixing metal ion solution at room temperature to create a cloudy solution.¹³ After the addition of the EDTA/NH₄OH mixture, the pH of this solution was then adjusted to 10 to ensure proper EDTA chelation with the metal ions.¹³

This solution was then heated to allow the chelates to undergo polyesterification with the metal atoms.¹³ The temperature of this solution was then increased to 90–100 °C to allow for the removal of excess water that resulted in a viscous gel.¹³ Continued heating resulted in the thermal decomposition of the gel to produce a fine black powder.¹³ The resulting powder was collected and calcined for 5 h at 1150 °C to oxidize excess organic residue and leave behind the phase pure material as determined by X-ray diffraction (XRD) conducted on a Siemens D-500 diffractometer, a Cu Kα radiation source, and a graphite diffracted beam monochromator.¹³

Diffraction studies were also performed on oxidized and reduced SFMO samples to verify phase stability. This was accomplished by pressing a 1 mm by 15 mm pellet of the SFMO at 10 000 psi for 5

min. These pellets were then put into a tube furnace and were heated under an air atmosphere at 800 °C for 24 h. The pellets were then removed and ground into a fine powder to be tested, at room temperature, with the XRD to obtain an oxidized scan. The powder was then repressed and was exposed to a reducing atmosphere of 5% H₂ diluted with argon for 24 h, which was then followed by ex situ analysis with the XRD. Rietveld refinement was done on the oxidized and reduced sample utilizing GSAS software.⁶¹ To ensure accurate measurements of the lattice parameters and to remove instrumental inconsistencies, an internal standard of anatase, TiO₂, was applied to both samples.

High Temperature X-ray Absorption Spectroscopy Chamber. A custom high temperature XAS electrochemical fixture was built to allow for the exploration of the SFMO materials at high temperatures (800 °C) and exposed to reducing and oxidizing atmospheres using fluorescence based XAS measurements.⁵¹ This system is equipped with a ceramic substrate heater that can heat a sample up to 1100 °C in oxidizing and reducing environments.⁵¹ This device also incorporates multiple, hermetic electrical feedthroughs that permit current to the furnace heating element and thermocouple monitoring of temperature.⁵¹ Inlet and outlet gas ports were also integrated into the chamber to control flow of either a reducing (3% H₂ in 97% He) or oxidizing (air) environment.⁵¹ There is a top removable flange that allows for new samples to be introduced and old samples to be removed.⁵¹ This chamber is also equipped with two X-ray transmissive Kapton windows positioned 90° from each other to allow for X-ray radiation to enter the chamber, interact with the sample, and allow fluorescence photons to leave the chamber to be recorded by a five grid fluorescence ion chamber (EXAFS Co.).⁵¹ A schematic of the described system can be seen in Figure 3.⁵¹

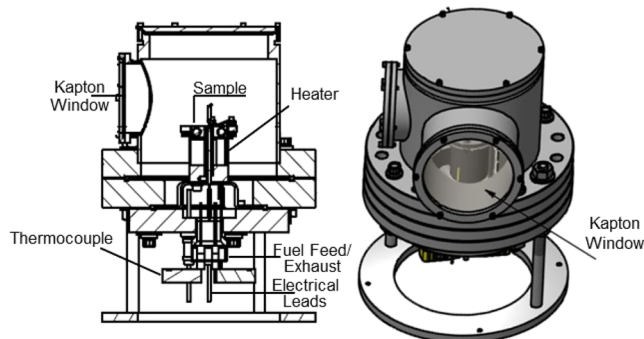


Figure 3. Schematic design of SOFC architecture used in majority of high temperature reactive XAS experiments. (Left) Cross section of chamber showing components. (Right) 3-D representation of high temperature XAS chamber. Reproduced with permission from ref 51. Copyright 2015 John Wiley and Sons.

XANES and EXAFS Studies of Sr₂Fe_{1.5}Mo_{0.5}O_{6-δ}. To investigate the limits of reduction and oxidation for SFMO at 800 °C, XAS measurements were taken of bulk SFMO pellets utilizing the high temperature XAS chamber. These measurements were taken at the Materials Research Collaborative Access Team (MRCAT) Sector 10-ID beamline at the Advanced Photon Source located at Argonne National Laboratory.⁶² The metals edges that were analyzed were the Fe K-edge around 7.112 keV and the Mo K-edge around 19.999 keV. Both of these edges were tuned to Fe and Mo foil standards prior to testing of the SFMO material. SFMO pellets were created by loading a 15 mm pressing die with 1 g of SFMO powder and pressing at 10 ksi for 5 min. The resulting pellet was sintered at 1200 °C in a muffle furnace. The pellet was mounted to the substrate heater in the high temperature XAS chamber and was heated to 800 °C under an oxidizing atmosphere, 200 sccm of compressed air. The incoming X-ray radiation had a grazing angle of 5° to the sample pellet surface. The fluorescence photons emitted from the sample were measured 90° from the X-ray radiation source at a 20° angle from the surface of the pellet. Continuous scan (~2 min) spectra were taken for 1 h to

ensure a steady state was reached for the oxidized SFMO sample. The chamber was then purged with helium to evacuate any air before a reducing atmosphere of 3% H₂ (diluted in helium) was applied to the chamber at 200 sccm to reduce the SFMO sample. Continuous spectra were once again taken for 1 h to ensure a steady state was reached for the reduced SFMO sample.

Because the sample is thick (1 mm) and concentrated in all the elements measured, self-absorption corrections were applied to both the XANES and EXAFS data.⁶³ The parameters used for the correction corresponded to the geometry of the high temperature chamber (5° incident angle, 20° exit angle), and the thickness of the sample was adjusted to ensure that the room temperature data matched the data taken on a powder sample in transmission. The same parameters were used for all the measurements of oxidized and reduced samples. More information regarding the self-absorption correction can be found in the Supporting Information along with a comparison of the corrected and uncorrected spectra with transmission data.

EXAFS Modeling. Initial processing of data was performed with the Athena program.⁶⁴ The spectra taken for each oxidation/reduction step were screened, and those that were collected at a steady state of full oxidation or reduction were merged to obtain better signal-to-noise. For XANES analysis, the merged spectra were normalized and corrected for self-absorption using the Fluorescence correction. For EXAFS analysis, the spectra were normalized, background was subtracted, and then the spectra were corrected for self-absorption using the Booth correction. Further details regarding the self-absorption corrections can be seen in the Supporting Information. The EXAFS data were fitted using the Artemis package based on IFEFFIT.^{64,65} The background subtracted spectra were Fourier transformed in the range $2 \text{ \AA}^{-1} < k < 10 \text{ \AA}^{-1}$ and fitted with a single path over the range $1 \text{ \AA} < R < 2 \text{ \AA}$ using a k^2 weighting.

RESULTS AND DISCUSSION

X-ray Diffraction Redox Studies. As a SOFC anode, SFMO has been coveted as a redox stable material.^{34,37–50} To explore this redox stability property further, initial X-ray diffraction studies were performed on the bulk SFMO material. In these measurements, an SFMO pellet was exposed to both reducing and oxidizing atmospheres at 800 °C. Between each step, the crystallinity of this pellet was tested with X-ray powder diffraction. This material showed stable crystallinity and phase purity through multiple redox cycles. This reversibility can be observed in Figure S1 of the Supporting Information.

From the diffraction patterns, shown in Figure 4, it is observed that whether reduced or oxidized, SFMO maintains its *Pnma* space group. However, slight changes were observed with the lattice parameters of this material as seen in Table 1. The main change that has occurred when SFMO was reduced was an increase in the lattice parameter “c” from 5.5506 to 5.5563 Å. The increase in c also leads to an increase in the total cell volume when the sample was reduced, most likely consistent with an expansion of the B-site metal octahedral complex as a result of a change in metal oxidation and/or oxygen concentration surround the atom. Neutron powder diffraction accompanied by computational studies performed by Munoz-Garcia et al. revealed that SFMO with the 3:1 ratio of Fe and Mo in the empirical formula has no apparent ordering of these metals in the B and B' sites of this crystal lattice.³⁴

High Temperature X-ray Absorption Redox Studies. The ex situ XRD studies on the reduced and oxidized samples of SFMO show that this material maintains its crystallographic phase under redox conditions. However, there are still key fundamental questions left unanswered, which include the

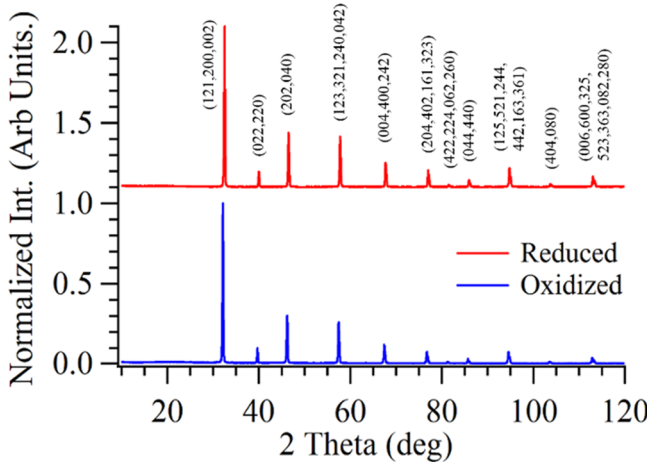


Figure 4. X-ray diffraction pattern for the single phase of the oxidized and reduced $\text{Sr}_2\text{Fe}_{1.5}\text{Mo}_{0.5}\text{O}_{6-\delta}$ (SFMO) perovskite material.

Table 1. Structural Refinement Results from the Reduced and Oxidized $\text{Sr}_2\text{Fe}_{1.5}\text{Mo}_{0.5}\text{O}_{6-\delta}$ (SFMO) Diffraction Patterns Displayed in Figure 4 and from Literature^{34,a}

lattice parameter	oxidized	reduced	literature ³⁴
<i>a</i> (Å)	5.5444 ± 0.0006	5.5441 ± 0.0014	5.5472
<i>b</i> (Å)	7.8375 ± 0.0007	7.8356 ± 0.0022	7.827
<i>c</i> (Å)	5.5506 ± 0.0005	5.5563 ± 0.0025	5.552
<i>V</i> (Å ³)	241.0564	241.3732	241.056

^aAll possess a *Pnma* space group. The literature values were determined for an oxidized SFMO sample.³⁴

following: (1) With minimal change in the SFMO crystal structure during oxidation and reduction, does this correlate to minimal oxidation state changes of the “B” site metals and in the formation of oxide vacancies in this material? (2) Do the room temperature ex situ findings represent the fundamental chemistry of this material at SOFC operational temperature of 800 °C? In order to address these questions, X-ray absorption spectroscopy (XAS) in combination with a custom-built high temperature XAS chamber was employed to explore the extent of oxidation and reduction of the SFMO material at 800 °C.

XAS spectra consist of two distinct sections: the XANES and EXAFS regions. The XANES region, ~40 eV around the absorption edge, contains information about the electronic structure of the absorbing atom which is specifically associated with formal oxidation states and the chemical bonding environment around the metal. The EXAFS region, which extends up to 1000 eV beyond the absorption edge, can be modeled to extract geometric information about the local structure (distances, number, and types of neighboring atoms) surrounding the absorbing atom.^{66–72} In this work, the Fe and Mo K-edges are measured, corresponding to the energy needed to photoionize an electron from the 1s state. For the oxidized SFMO sample the Fe edge energy occurs at 7.127 keV, and for Mo the edge is located at 20.016 keV. In the XANES portion of this spectrum there can also be restricted transitions that show up in the “pre-edge” region of the spectrum that are associated with a quadrupole-allowed transitions due to crystalline electric fields resulting from near neighbor bonds. The combination of XANES and EXAFS will be used to explore the extent of oxidation state changes in the Fe and Mo atoms and the origins of oxygen vacancy formations in SFMO.

As an anode material exposed to the reducing fuel atmospheres of SOFCs, a perovskite must possess multivalent “B” sites in order to provide a pathway for electron conduction through the differing energies of the metal conduction bands. In order to understand the extent of the roles that Fe and Mo will play in the electron conduction mechanism, the XANES spectra for the Fe and Mo K-edges were analyzed for both oxidized and reduced SFMO samples to monitor oxidation state changes. Just as with the XRD studies, SFMO was exposed to multiple redox cycles for XAS analysis to exhibit the remarkable ability of this material to be stable in both oxidizing and reducing environments. These XAS data for both the Fe and Mo K-edges can be seen in **Figure S2 in the Supporting Information**.

Fe K-Edge Analysis. The oxidation states of Fe in SFMO have been extensively studied by other researchers with the use of X-ray photoelectron spectroscopy.^{34,37–50} The observations from these studies have provided varying results about the actual oxidation state of Fe when SFMO is at room temperature and in the fully oxidized state. Researchers like Liu et al. reported that the Fe favors the +2 oxidation state and Wang et al. have reported that 92.4% of the Fe will assume the +2 state while only 7.6% will assume the +3 state,^{37,46} while other researchers including Li et al. and Xiao et al. have reported that the average oxidation state of Fe in SFMO is +3.16 from varying contributions of +2, +3, and +4 oxidation states.^{47,48} Some other researchers have seen an almost near equal contribution of Fe^{2+} and Fe^{3+} for this material to produce an average oxidation state closer to +2.5.^{38–41}

When trying to understand how the Fe in SFMO will respond to SOFC operating conditions, Liu et al. had also used a high temperature XPS stage to test the SFMO material at 550 °C while under low torr reducing conditions.⁴⁵ These findings indicated that the oxidized SFMO has Fe fully in the +3.00 oxidation state but observes a shift to an average oxidation state of +2.67 (67.6% Fe^{3+} and 32.4% Fe^{2+}) when exposed to this high temperature reducing environment.⁴⁵

In these present studies we are utilizing XAS with a custom chamber to expose SFMO to more realistic SOFC operation conditions of 800 °C while exposed to reducing and oxidizing conditions at 1 atm. The high temperature Fe K-edge XANES spectra for oxidized and reduced samples compared to standard spectra are shown in **Figure 5**. There are noticeable

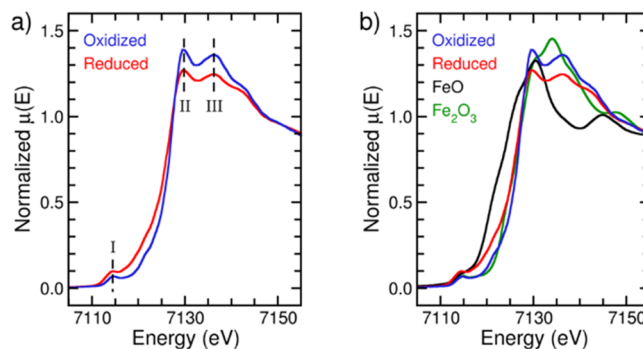


Figure 5. (a) Fe K-edge XANES spectra of reduced and oxidized $\text{Sr}_2\text{Fe}_{1.5}\text{Mo}_{0.5}\text{O}_{6-\delta}$ (SFMO) samples taken at 800 °C. Highlighted are the pre-edge (I) peak and the peaks associated with the 1s to $4p_{1/2}$ (II) and the 1s to $4p_{3/2}$ (III) transitions. (b) Comparison of the oxidized and reduced SFMO spectra to room temperature XAS spectra of the standards FeO and Fe_2O_3 .

changes that occur for the reduced SFMO Fe K-edge spectrum when compared to the oxidized spectrum. There is a slight shift in the Fe K-edge energy from 7.1270 keV for the oxidized sample to 7.1259 keV for the reduced sample. When compared to Fe (2+) and Fe (3+) standards, it is observed that the edge energy for the oxidized sample falls in the vicinity of Fe_2O_3 and assumes an oxidation state of +3.04 (Figure 5b). For the reduced sample the Fe edge energy still falls in the vicinity of the Fe (3+) standard, but the shift in the edge energy for the reduced sample correlates to a possible slight oxidation state change to +2.75. This Fe oxidation state is in good agreement with the results of XPS studies of Liu et al.⁴⁵

The Fe K-edge XANES peaks associated with the $\text{Fe} 1s \rightarrow 4p_{1/2}$ and $1s \rightarrow 4p_{3/2}$ electron transitions, highlighted in Figure 5a with a “II” and “III”, show no shift. This lack of energy change for these transitions could indicate that the Fe atoms in SFMO are most likely not changing their oxidation state. In addition, the pre-edge peak assigned to the $1s \rightarrow 3d$ transition also exhibits no shift in energy. Other crystallographic effects, other than metal oxidation state, have been known to shift the edge energy.^{71,72} These effects can include the coordination and geometry of the neighboring atoms, spin states of the electronic transitions, and the extent of 3d–4p mixing brought upon by oxygen’s 2p orbital. Thus, the XANES data could be indicative of a change in the oxygen environment around the Fe atoms brought upon by the creation of oxygen vacancies.

Extensive computational studies, performed by Munoz-Garcia et al., investigated the origins of oxygen vacancies in SFMO and the distribution of the extra electron density once the metal–oxygen bonds are broken.^{34,44} Theoretically to maintain charge neutrality, the oxygen stoichiometry in SFMO should be 5.75 with $\delta = 0.25$. However, experimentally they observed an oxygen stoichiometry of 5.90 with $\delta = 0.10 \pm 0.02$ with powder neutron diffraction data.^{34,44} In both of these δ cases they studied the three main possibilities for oxygen vacancy formation ($\text{V}_{..}$) to occur across the $\text{Fe}-\text{O}-\text{Fe}$, $\text{Fe}-\text{O}-\text{Mo}$, and $\text{Mo}-\text{O}-\text{Mo}$ bonds. It was observed that the E_{form} of $\text{Fe}-\text{V}_{..}-\text{Fe}$ and $\text{Fe}-\text{V}_{..}-\text{Mo}$ is only feasible for this crystal system due to a significantly weaker Fe–O bond strength. Once the neutral oxygen atom leaves the crystal lattice, the extra electrons associated with the formal O^{2-} atom are then redistributed through the SFMO lattice.^{34,44}

A qualitative view of this redistribution of electron density was obtained by understanding the level of iconicity and covalency of these metal–oxygen bonds through the investigation of the Bader charges on the atoms in SFMO.^{34,44} It was found that the Fe–O and Mo–O bonds had a high level of covalency that can enhance the electron redistribution through this material. Their computational models observed that minimal electron charge is redistributed directly to the Fe atom and the redistribution of charge was favored for the Mo atom.^{34,44} The main reason for Fe not gaining electrons during oxygen vacancy formation is that when Fe is in the +3 oxidation state, it has d^5 high spin electron configuration. This d^5 electron configuration allows for lowest electron–electron repulsion and explains why there is no motivation for Fe^{3+} to further reduce to the Fe^{2+} .^{34,44} Instead, the extra electron density forming between the Fe atoms ($\text{Fe}-\text{V}_{..}-\text{Fe}$) will redistribute to the surrounding oxygen atoms. This redistribution is made possible by the direct overlap of Fe 3d orbitals with O 2p orbitals in the crystal lattice that form σ and π orbitals that allow for electron transport between these atoms.^{34,44}

It was shown by the previous explained publication that Fe should remain in the +3 oxidation state even when oxygen vacancies are forming in SFMO.^{34,44} In these experiments Fe oxidation state changes from +3.04 to +2.75 when exposed to a reducing atmosphere, shown in Figure 5. This slight change in oxidation state could be attributed to the loss of the electron withdrawing oxygen atoms from the highly covalent system as opposed to Fe gaining electrons which was also seen in the computational work of Munoz-Garcia et al.^{34,44} This was suggested by the overlapping Fe electronic transitions in the reduced and oxidized XANES spectra also observed in Figure 5. To further confirm if the oxygen environment around the Fe atom is changing when exposed to oxidizing and reducing atmospheres, the Fe K-edge EXAFS data in both oxidized and reduced states were fitted, and the results are shown in Figure 6.

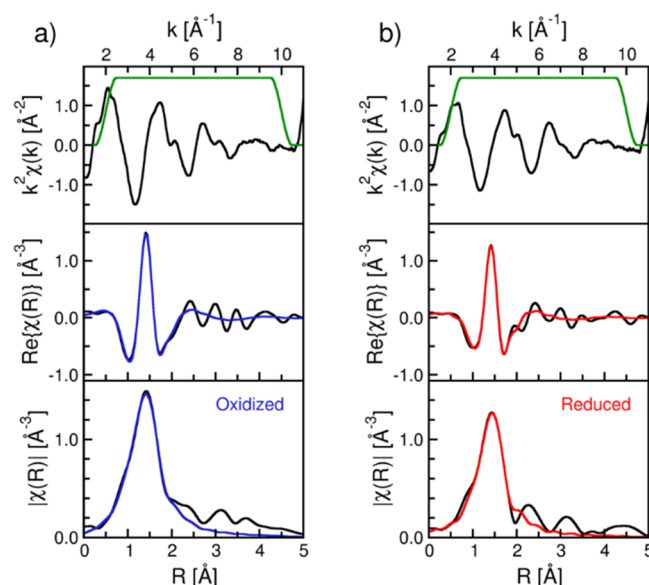


Figure 6. Fit results for the first shell EXAFS modeling of the Fe K-edge for (a) oxidized and (b) reduced samples of SFMO. The top panel shows the k^2 -weighted $\chi(k)$ and the Fourier transform window. The middle and bottom panels show the real part and the magnitude of the Fourier transform (black) and the fits (color), respectively.

The high temperature environments of these measurements are reflected in a large thermal disorder, limiting the modeling to a single Fe–O path and only first-shell analysis. This limited analysis is sufficient for these studies as all the atoms in the first shell are oxygen and provide information about the possibility of the formation of oxygen vacancies around Fe. The results of these fit are presented in Table 2. To provide a qualitative view in the formation of oxygen vacancies, a single path of Fe–O was modeled and the number of oxygens, “ N ”, around the Fe atom in the oxidized samples was fixed at 6.0 to obtain a value for the amplitude reduction factor S_0^{-2} . This obtained S_0^{-2} was then held constant for the reduced sample while other parameters were allowed to vary for the EXAFS modeling. It is notable that there is no significant change in the Fe–O bond length which is unchanged at 1.93 Å. This constant bond length for the oxidized and reduced SFMO samples further confirms that the Fe atom does not change its oxidation state, which would have resulted in a changing ionic radius and consequent bond length change. The EXAFS modeling further

Table 2. Fit Results for the First Shell EXAFS Modeling of Fe and Mo K-Edges

EXAFS parameter	oxidized	reduced
Fe EXAFS		
R (Å)	1.92 ± 0.02	1.93 ± 0.02
N	6.0	4.0 ± 0.6
σ^2	0.014 ± 0.003	0.009 ± 0.003
E_0	1.0	2.5
Mo EXAFS		
R (Å)	1.88 ± 0.03	1.93 ± 0.02
N	6.0	5.2 ± 0.9
σ^2	0.006 ± 0.005	0.005 ± 0.003
E_0	8.2	9.3

reveals that the number of oxygens in the octahedral complex decreases to 4.0 ± 0.6 in reducing environments. This decrease in “N” correlates to the edge shift seen for the Fe K-edge in Figure 5 for the reduced sample because electron withdrawing oxygens atoms are leaving the system. It was also observed that there is a high mean square displacement, “ σ^2 ”, for oxidized SFMO which could correlate to two separate Fe–O distances. These two separate Fe–O distances could be attributed to the two possible paths that oxygen vacancies can form, which are Fe–O–Fe and Fe–O–Mo. For the reduced sample, the σ^2 significantly decreases suggesting that there is only a single Fe–O bond length, which could denote a loss of axial oxygens in the FeO_6 octahedral while leaving behind the equatorial oxygens in a square planar geometry.

Mo K-Edge Analysis. Just as with the Fe K-edge, there is a noticeable change in the Mo K-edge when the SFMO sample is exposed to a reducing atmosphere at 800 °C, Figure 7. It is

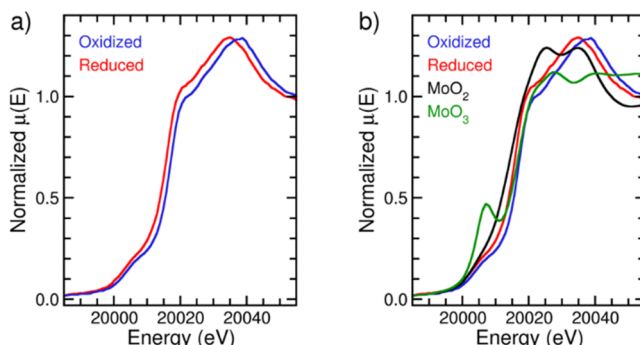


Figure 7. (a) Mo K-edge XANES spectra of reduced and oxidized $\text{Sr}_2\text{Fe}_{1.5}\text{Mo}_{0.5}\text{O}_{6-\delta}$ (SFMO) samples taken at 800 °C. (b) Comparison of the oxidized and reduced SFMO spectra to room temperature XAS spectra of the standards MoO_2 and MoO_3 .

observed that the Mo edge energy changes from 20.0161 keV for oxidized SFMO to 20.0151 keV when it is reduced. When compared to MoO_2 and MoO_3 standards, the Mo K-edge energy for oxidized SFMO can be assigned a +5.88. When the SFMO sample is reduced, the edge energy shifts to an oxidation state to +5.14, Figure 7b. In similar high temperature XPS studies performed by Liu et al., a shift in the Mo oxidation state in the reduced SFMO sample from +6.00 to +5.39 was observed.⁴⁵ The percentages of Mo^{6+} and Mo^{5+} for the SFMO reduced sample were observed to be 38.9% and 61.1%.⁴⁵ It is observed that our SFMO sample described in these studies is able to enter into an even lower oxidation state of +5.14,

which could be a factor of being closer to the higher SOFC operation temperatures of 800 °C.

Unlike with the Fe XANES analysis, when investigating the peaks assigned to the $1s \rightarrow 4p$ transitions, there is now an apparent shift from the oxidized to the reduced state, supporting the hypothesis that there is an actual oxidation state change in the Mo atoms. This ability for Mo to obtain electrons in the crystal structure over the Fe atoms could be attributed to its higher electron affinity at 72.10 kJ/mol which is significantly greater than Fe at 14.79 kJ/mol. This ability for Mo to gain electrons was also observed by Munoz-Garcia et al. in their performed first-principle computational studies.^{34,44} Unlike the low electron–electron repulsion seen in the Fe^{3+} electron configuration (d^5), the Mo^{6+} has a d^0 electron configuration which allows for the reduction of Mo to the +5 or +4 oxidation state without any penalties from electron repulsion.^{34,44}

To investigate if the Mo atoms in SFMO play a role in oxide vacancy formation for this material, similar first shell EXAFS modeling was conducted on the Mo K-edge spectra. The fits of this model to the experimental data can be seen in Figure 8

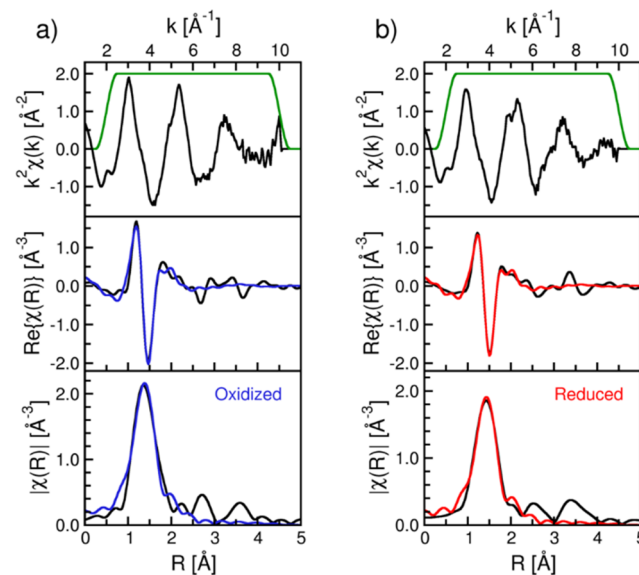


Figure 8. Fit results for the first shell EXAFS modeling of the Mo K-edge for (a) oxidized and (b) reduced samples of SFMO. The top panel shows the k^2 -weighted $\chi(k)$ and the Fourier transform window. The middle and bottom panels show the real part and the magnitude of the Fourier transform (black) and the fits (color), respectively.

along with the fit results reported in Table 2. It is observed that Mo also suffers from the same high temperature dampening of the EXAFS signal as was seen with the Fe data. When the SFMO material becomes reduced, a change in the Mo–O bond length is observed from 1.88 Å for the oxidized sample to 1.93 Å for the reduced sample. This expansion of the Mo–O bond supports the finding in the XANES data which showed that the Mo oxidation state was reducing leading to a larger atomic radius and in turn a longer resulting bond length.

A change in the number of oxygen atoms is observed at 5.2 ± 0.9 when the sample is reduced. However, with the large error in this “N” parameter, this number is statistically identical to the six oxygens for the oxidized sample. This suggests that Mo is less likely, when compared to Fe, to form oxygen vacancies in the crystal structure of SFMO. The high error in N

could also be attributed to the low concentration of Mo in SFMO compared to Fe. Comparing the relative bond strength of Fe–O at 407 kJ/mol to the larger bond strength of 502 kJ/mol for Mo–O, it is reasonable to conclude that Fe is primarily responsible for the formation of oxygen vacancies in the SFMO material. This slight lower number in oxygen around Mo could be attributed to the loss of oxygens that are also attached to Fe atoms (Fe–O–Mo) which was found to be a viable option for oxygen vacancy formation due to low E_{form} .^{34,44} Since Fe in SFMO is repelling this electron charge to surrounding oxygen atoms, this would explain how this electronic charge can be redistributed to the Mo atom.

CONCLUSIONS

The mixed ionic and electronic conducting capability of $\text{Sr}_2\text{Fe}_{1.5}\text{Mo}_{0.5}\text{O}_{6-\delta}$ was explored with high temperature X-ray absorption spectroscopy to mimic how this anode material will behave under SOFC operational conditions and temperatures of 800 °C. Specifically, the local electronic structure of the Fe and Mo “B” site metals in SFMO was explored with XANES measurements for oxidized and reduced samples. In addition, the oxidized and reduced SFMO samples were also explored for their potential to form oxygen vacancies around these same “B” site metals with EXAFS studies. Understanding the MIEC properties of this material will provide insight into how SFMO can act as an effective anode catalyst toward hydrocarbon fuels.

Initial XRD studies showed an expansion of the SFMO crystal lattice when this material was exposed to reducing conditions. The high temperature XAS studies show that both Fe and Mo play a role in this expansion but in complementary ways. The XANES studies of the Fe K-edge revealed a change in the surrounding oxygen content that resulted in an edge energy shift. EXAFS analysis of the Fe data verified significant oxygen vacancies in the reduced state. The electrons returned to the crystal lattice by the vacancies are attracted to the Mo atom (instead of Fe) because of their high electron affinity, d^5 electron configuration, and a high level of covalency to the Fe–O bond. This is reflected in the shift of Mo XANES spectrum and the Mo EXAFS results which show a Mo–O bond length expansion but with minimal oxygen vacancies due to a high Mo–O bond strength. The expansion of the SFMO lattice, under reducing conditions, seen in the XRD results is attributed to a series of processes. This is first started by the creation of oxygen vacancies surrounding the Fe atoms which initiates a redistribution of electrons to the Mo atoms that causes a distortion of the MoO_6 octahedral from a lengthening of the Mo–O bond length.

These results have provided an important insight into the complementary roles that Fe and Mo play in the ionic and electronic conducting properties of this material. Fe is primarily responsible for oxygen ion conduction due the significant vacancy formation in its local environment, while Mo plays a more significant role in the conduction of electrons through its superior ability to attract electrons and accommodate valence changes. However, this is a multistep process that first starts with an oxygen vacancy either forming across the Fe–V···Fe or the Fe–V···Mo bond. Two electrons will be left to be redistributed through the SFMO lattice though overlapping Fe 3d and O 2p orbitals to where they arrive at the Mo atoms to cause reduction to drive Mo into the +5 and +4 oxidation states.³⁴

Previous studies have shown that this SFMO anode catalyst can operate with hydrocarbon fuels that are known to form

detrimental graphite deposits.¹³ These high temperature reactive XAS studies provided a unique perspective into the roles that B site metals play in the mixed ionic and electronic conducting properties of this perovskite. Specifically, these studies revealed the origins of oxygen vacancy formation that can induce oxide ionic conduction through the SFMO material to resist graphite formation.¹³ The ability to conduct measurements of this kind under SOFC operational conditions can now provide a better understanding of the fundamental perovskite anode catalyst chemistry that is occurring in these SOFC devices and will assist in the future development of effective and fuel efficient SOFC devices.

ASSOCIATED CONTENT

Supporting Information

The Supporting Information is available free of charge on the ACS Publications website at DOI: [10.1021/acsaem.8b01579](https://doi.org/10.1021/acsaem.8b01579).

Additional figures exhibiting the reversibility of the XRD, XANES, and EXAFS ([PDF](#))

AUTHOR INFORMATION

Corresponding Author

*E-mail: bryan.eigenbrodt@villanova.edu.

ORCID

Carlo U. Segre: [0000-0001-7664-1574](https://orcid.org/0000-0001-7664-1574)

Bryan C. Eigenbrodt: [0000-0001-9782-5321](https://orcid.org/0000-0001-9782-5321)

Funding

The authors greatly acknowledge funding and support from the Argonne National Laboratory through the General Users Proposal GUP-30910 which provided access and beamtime at their Advanced Photon Source (APS) to conduct these experiments. Jeremy P. Carlo acknowledges support from the Research Corporation for Science Advancement, Cottrell College Science Award 23314. Travel expenses to bring researchers to the APS at ANL were provided by Villanova University through their University Summer Research Fellowship Program. Additional support was provided through and Educational Partnership Award with the Air Force Office of Scientific Research (Grant 13-EPA-RQ-11). Travel funds for this project were provided by Villanova University through the University Summer Grant program.

Notes

The authors declare no competing financial interest.

ACKNOWLEDGMENTS

The authors gratefully acknowledge support from Argonne National Laboratory through the Advanced Photon Source General User Proposal (GUP-30910) to provide the beamtime at the Material Research Collaborative Access Team (MRCAT) 10-ID beamline. MRCAT operations are supported by the Department of Energy (DOE) and the MRCAT member institutions. This research used resources of the Advanced Photon Source, a U.S. Department of Energy Office of Science User Facility operated for the DOE Office of Science by Argonne National Laboratory under Contract DE-AC02-06CH11357.

REFERENCES

- (1) Ormerod, R. Solid oxide fuel cells. *Chem. Soc. Rev.* **2003**, *32*, 17–28.

- (2) Song, C. Fuel Processing for low-temperature and high temperature fuel cells: challenges, and opportunities, for sustainable development in the 21st century. *Catal. Today* **2002**, *77*, 17–49.
- (3) Pomfret, M.; Demircan, O.; Sukeshini, A.; Walker, R. Fuel oxidation efficiencies and exhaust composition in solid oxide fuel cells. *Environ. Sci. Technol.* **2006**, *40*, 5574–5579.
- (4) Atkinson, A.; Barnett, S.; Gorte, R.; Irvine, J.; McEvoy, A.; Mogensen, M.; Singhal, S.; Vohs, J. Advanced anodes for high temperature fuel cells. *Nat. Mater.* **2004**, *3*, 17–27.
- (5) Eigenbrodt, B.; Pomfret, M.; Steinhurst, D.; Owrtusky, J.; Walker, R. Direct, *in situ* optical studies of solid oxide fuel cells operating with methanol and methane. *J. Phys. Chem. C* **2011**, *115*, 2895–2903.
- (6) McIntosh, S.; He, H.; Lee, S.; Costa-Nunes, O.; Krishnan, V.; Vohs, J.; Gorte, R. An examination of carbonaceous deposits in direct-utilization SOFC anodes. *J. Electrochem. Soc.* **2004**, *151*, A604–8.
- (7) McIntosh, S.; Vohs, J.; Gorte, R. Role of hydrocarbon deposits in the enhanced performance of direct oxidation SOFCs. *J. Electrochem. Soc.* **2003**, *150*, A470–6.
- (8) Pomfret, M.; Steinhurst, D.; Kidwell, D.; Owrtusky. Thermal imaging of solid oxide fuel cells anode processes. *J. Power Sources* **2010**, *195*, 257–62.
- (9) Dokmaingam, P.; Assabumrungrat, S.; Soottitantawat, A.; Laosiripojana, N. Modeling of tubular-designed solid oxide fuel cell with indirect internal reforming operation fed by different primary fuels. *J. Power Sources* **2010**, *195*, 69–78.
- (10) Sun, C.; Stimming, U. Recent anode advances in solid oxide fuel cells. *J. Power Sources* **2007**, *171*, 247–60.
- (11) Gong, M.; Liu, X.; Trembley, J.; Johnson, C. Sulfur tolerant anode materials for solid oxide fuel cell application. *J. Power Sources* **2007**, *168*, 289–298.
- (12) Huang, Y.; Dass, R.; Xing, Z.; Goodenough, J. Double perovskite as anode materials for solid oxide fuel cells. *Science* **2006**, *312*, 254–7.
- (13) Bode, G.; McIntyre, M.; Neuberger, D.; Walker, R.; Thorstensen, B.; Eigenbrodt, B. Electrochemical and Operando Spectroscopic Studies of $\text{Sr}_2\text{Fe}_{1.5}\text{Mo}_{0.5}\text{O}_{6-\delta}$ Anode Catalyst in Solid Oxide Fuel Cells Operating with Direct Alcohol Fuels. *ChemElectroChem* **2018**, *5* (21), 3162–3168.
- (14) Goodenough, J. Oxide ion electrolytes. *Annu. Rev. Mater. Res.* **2003**, *33*, 91–128.
- (15) Hui, S.; Petric, A. Electrical properties of yttrium doped strontium titanate under reducing conditions. *J. Electrochem. Soc.* **2002**, *149*, J1–10.
- (16) Ihara, M.; Hasegawa, S. Quickly rechargeable direct carbon solid oxide fuel cell with propane for recharging. *J. Electrochem. Soc.* **2006**, *153*, A1544–46.
- (17) Pomfret, M.; Stoltz, C.; Varughese, B.; Walker, R. Structural and compositional characterization of yttria-stabilized zirconia: evidence of surface-stabilized, low-valence metal species. *Anal. Chem.* **2005**, *77*, 1791–1795.
- (18) Swider, K.; Worrell, W. Electronic conduction mechanism in yttria-stabilized zirconia-titania under reducing atmospheres. *J. Electrochem. Soc.* **1996**, *143*, 3706–3711.
- (19) Decaluwe, S.; Zhu, H.; Kee, R.; Jackson, G. Importance of anode microstructure in modeling solid oxide fuel cells. *J. Electrochem. Soc.* **2008**, *155*, B538–B546.
- (20) Zhu, H.; Kee, R. Modeling electrochemical impedance spectra in SOFC button cells with internal methane reforming. *J. Electrochem. Soc.* **2006**, *153*, A1765–72.
- (21) Ma, Y.; Li, Y.; Liu, T.; Zhao, X.; Zhang, L.; Han, S.; Wang, Y. Enhanced hydrogen storage properties of LiBH_4 generated using a porous Li_3BO_3 catalyst. *J. Alloys Compd.* **2016**, *689*, 187–191.
- (22) Li, W.; Zhang, B.; Yuan, J.; Yan, Y.; Wu, Y. Effects of Mo content on the microstructure and electrochemical performances of $\text{La}_{0.75}\text{Mg}_{0.25}\text{Ni}_{3.2-x}\text{Co}_{0.2}\text{Al}_{0.1}\text{Mo}_x$ ($x = 0, 0.10, 0.15, 0.20$) hydrogen storage alloys. *J. Alloys Compd.* **2017**, *692*, 817–824.
- (23) Malyshkin, D.; Novikov, A.; Tsvetkov, D.; Zuev, A. Preparation, oxygen nonstoichiometry and defect structure of double perovskite $\text{LaBaCo}_2\text{O}_6$. *Mater. Lett.* **2018**, *229*, 324–326.
- (24) Sayagues, M.; Gotor, F.; Pueyo, M.; Poyato, P.; Garcia-Garcia, F. J. Mechanosynthesis of $\text{Sr}_{1-x}\text{La}_x\text{TiO}_3$ anodes for SOFCs: Structure and electrical conductivity. *J. Alloys Compd.* **2018**, *763*, 679–686.
- (25) Kwon, O.; Kim, K.; Joo, S.; Jeong, H.; Shin, J.; Han, J.; Sengodan, S.; Kim, G. Self-assembled alloy nanoparticles in a layered double perovskites as a fuel oxidation catalyst for solid oxide fuel cells. *J. Mater. Chem. A* **2018**, *6*, 15947–15953.
- (26) Sarno, C.; Luisetto, I.; Zurlo, F.; Licoccia, S.; Di Bartolomeo, E. Lanthanum chromite based composite anodes for dry reforming of methane. *Int. J. Hydrogen Energy* **2018**, *43*, 14742–14750.
- (27) Cimenti, M.; Hill, J. Direct utilization of methanol on impregnated Ni/YSZ and $\text{Ni-Zr}_{0.35}\text{Ce}_{0.65}\text{O}_2$ /YSZ anodes for solid oxide fuel cells. *J. Power Sources* **2010**, *195*, 3996–4001.
- (28) Cimenti, M.; Hill, J. Thermodynamic analysis of solid oxide fuel cells operated with methanol and ethanol under direct utilization, steam reforming, dry reforming or partial oxidation conditions. *J. Power Sources* **2009**, *186*, 377–384.
- (29) Hauptmeier, K.; Penkuhn, M.; Tsatsaronis, G. Economic assessment of a solid oxide fuel cell system for biogas utilization in sewage plants. *Energy* **2016**, *117*, 361–368.
- (30) Pomfret, M.; Steinhurst, D.; Owrtusky, J. Ni/YSZ solid oxide fuel cell anodes operating on humidified ethanol fuel feeds: an optical study. *J. Power Sources* **2013**, *233*, 331–340.
- (31) Howell, T.; Kuhnle, C.; Reitz, T.; Eigenbrodt, B.; Singh, R. $\text{Sr}_{2-x}\text{LaxMgMoO}_6$ and $\text{Sr}_{2-x}\text{LaxMgNbO}_6$ for use as sulfur-tolerant anodes without a buffer layer. *J. Am. Ceram. Soc.* **2014**, *97*, 3636–3642.
- (32) Howell, T.; Kuhnle, C.; Reitz, T.; Sukeshini, A.; Singh, R. $\text{A}_{(2)}\text{MgMoO}_{(6)}$ ($\text{A} = \text{Sr}, \text{Ba}$) for use as sulfur tolerant anodes. *J. Power Sources* **2013**, *231*, 279–284.
- (33) Liu, Q.; Xiao, G.; Howell, T.; Reitz, T.; Chen, F. A novel redox stable catalytically active electrode for solid oxide fuel cells. *ECS Trans.* **2011**, *35*, 1357–1366.
- (34) Munoz-Garcia, A.; Bugaris, D.; Pavone, M.; Hodges, J.; Huq, A.; Chen, F.; zur Loye, H.-C.; Carter, E. Unveiling structure-property relationships in $\text{Sr}_2\text{Fe}_{1.5}\text{Mo}_{0.5}\text{O}_{6-\delta}$ an electrode material for symmetric solid oxide fuel cells. *J. Am. Chem. Soc.* **2012**, *134*, 6826–6833.
- (35) Wang, Z.; Tian, Y.; Li, Y. Direct CH_4 fuel cell using $\text{Sr}_2\text{FeMoO}_6$ as an anode material. *J. Power Sources* **2011**, *196*, 6104–6109.
- (36) Xiao, G.; Chen, F. Ni modified ceramic anodes for direct-methane solid oxide fuel cells. *Electrochim. Commun.* **2011**, *13*, 57–59.
- (37) Wang, S.; Hsu, Y.; Huang, M.; Chang, C.; Cheng, S. Characteristics of Copper-Doped $\text{SrFe}_{0.75}\text{Mo}_{0.25}\text{O}_{3-\delta}$ Ceramic as a Cathode Material for Solid Oxide Fuel Cells. *Solid State Ionics* **2016**, *296*, 120–126.
- (38) Yang, G.; Feng, J.; Sun, W.; Dai, N.; Hou, M.; Hao, X.; Qiao, J.; Sun, K. The Characteristic of Strontium-Site Deficient Perovskite $\text{Sr}_{2-x}\text{Fe}_{0.75}\text{Mo}_{0.25}\text{O}_{3-\delta}$ ($x=1.9-2.0$) as Intermediate-Temperature Solid Oxide Fuel Cell Cathodes. *J. Power Sources* **2014**, *268*, 771–777.
- (39) Song, Y.; Zhong, Q.; Tan, W.; Pan, C. Effect of Cobalt-Substitution $\text{Sr}_2\text{Fe}_{1.5-x}\text{Co}_x\text{Mo}_{0.5}\text{O}_{6-\delta}$ for Intermediate Temperature Symmetrical Solid Oxide Fuel Cells Fed with $\text{H}_2\text{-H}_2\text{S}$. *Electrochim. Acta* **2014**, *139*, 13–20.
- (40) Dai, N.; Feng, J.; Wang, Z.; Jiang, T.; Sun, W.; Qiao, J.; Sun, K. Synthesis and Characterization of B-Site Perovskite $\text{Sr}_2\text{Fe}_{1.5-x}\text{Ni}_x\text{Mo}_{0.5}\text{O}_{6-\delta}$ ($x = 0, 0.05, 0.1, 0.2, 0.4$) as Cathodes for SOFCs. *J. Mater. Chem. A* **2013**, *1*, 14147–14153.
- (41) Qiao, J.; Chen, W.; Wang, W.; Wang, Z.; Sun, W.; Zhang, J.; Sun, K. The Ca Element effect on the enhancement performance of $\text{Sr}_2\text{Fe}_{1.5}\text{Mo}_{0.5}\text{O}_{6-\delta}$ Perovskite as Cathode for Intermediate-Temperature Solid Oxide Fuel Cells. *J. Power Sources* **2016**, *331*, 400–407.
- (42) Meng, J.; Liu, X.; Han, B.; Bai, Y.; Yao, C.; Deng, Niu, X.; Wu, X.; Meng, J. Improved Electrochemical Performance by Doping Cathode Materials $\text{Sr}_2\text{Fe}_{1.5}\text{Mo}_{0.5-x}\text{Ta}_x\text{O}_{6-\delta}$ ($0.0 \leq x \leq 0.15$) For Solid State Fuel Cell. *J. Power Sources* **2014**, *247*, 845–851.

- (43) Pan, X.; Wang, Z.; He, B.; Wang, S.; Wu, X.; Xia, C. Effect of Co Doping on the Electrochemical Properties of $\text{Sr}_2\text{Fe}_{1.5}\text{Mo}_{0.5}\text{O}_6$ Electrode for Solid Oxide Fuel Cell. *Int. J. Hydrogen Energy* **2013**, *38*, 4108–4115.
- (44) Munoz-Garcia, A.; Pavone, M.; Ritzmann, A.; Carter, E. Oxide Ion Transport in $\text{Sr}_2\text{Fe}_{1.5}\text{Mo}_{0.5}\text{O}_{6-\delta}$ a Mixed Ion-Electron Conductor: New Insight from First Principle Modeling. *Phys. Chem. Chem. Phys.* **2013**, *15*, 6250–6259.
- (45) Liu, Q.; Bugaris, D.; Xiao, G.; Chmara, M.; Ma, S.; zur Loye, H.-C.; Amiridis, M.; Chen, F. $\text{Sr}_2\text{Fe}_{1.5}\text{Mo}_{0.5}\text{O}_{6-\delta}$ as a Regenerative Anode for Solid Oxide Fuel Cells. *J. Power Sources* **2011**, *196*, 9148–9153.
- (46) Liu, Q.; Dong, X.; Xiao, G.; Zhao, F.; Chen, F. A Novel Electrode Material for Symmetrical SOFCs. *Adv. Mater.* **2010**, *22*, 5478–5482.
- (47) Li, Y.; Chen, X.; Yang, Y.; Jiang, Y.; Xia, C. Mixed-Conductor $\text{Sr}_2\text{Fe}_{1.5}\text{Mo}_{0.5}\text{O}_{6-\delta}$ as Robust Fuel Cell Electrode for Pure CO_2 Reduction in Solid Oxide Electrolysis Cell. *ACS Sustainable Chem. Eng.* **2017**, *5*, 11403–11412.
- (48) Xiao, G.; Wang, S.; Lin, Y.; Yang, Z.; Han, M.; Chen, F. Ni-Doped SrFeMoO as Anode Materials for Solid Oxide Fuel Cells. *J. Electrochem. Soc.* **2014**, *161*, F305–F310.
- (49) Xiao, G.; Liu, Q.; Wang, S.; Komvokis, V.; Amiridis, M.; Heyden, A.; Ma, S.; Chen, F. Synthesis and Characterization of Mo-Doped $\text{SrFeO}_{3-\delta}$ as Cathode Materials for Solid Oxide Fuel Cells. *J. Power Sources* **2012**, *202*, 63–69.
- (50) Goodenough, J.; Huang, Y. Alternative Anode Material for Solid Oxide Fuel Cells. *J. Power Sources* **2007**, *173*, 1–10.
- (51) Eigenbrodt, B. C.; Young, A. M.; Howell, T. G.; Segre, C. U.; Reitz, T. L. High-Temperature, In Situ X-Ray Absorption Study of $\text{Sr}_2\text{MgMoO}_6$ Solid Oxide Fuel Cell Anode Materials. *ChemElectroChem* **2015**, *2*, 1568–1575.
- (52) Nielsen, J.; Jacobsen, T. Three phase boundary dynamics at metal/YSZ microelectrodes. *Solid State Ionics* **2008**, *178*, 1769–1776.
- (53) Pomfret, M.; Owrusky, J.; Walker, R. High temperature Raman spectroscopy of solid oxide fuel cell materials and processes. *J. Phys. Chem. B* **2006**, *110*, 17305–8.
- (54) Bebelis, S.; Neophytides, S. AC impedance study of Ni-YSZ cermet anodes in methane-fueled internal reforming YSZ fuel cells. *Solid State Ionics* **2002**, *152–153*, 447–453.
- (55) Bieberle, A.; Meier, L.; Gauckler, L. The electrochemistry of Ni pattern anodes used as solid oxide fuel cell model electrodes. *J. Electrochem. Soc.* **2001**, *148*, A646.
- (56) Bieberle, A.; Meier, L.; Gauckler, L. State-space modeling of the anodic SOFC system Ni, $\text{H}_2\text{-H}_2\text{O/YSZ}$. *Solid State Ionics* **2002**, *146*, 23.
- (57) Eigenbrodt, B.; Kirtley, J.; Walker, R. In situ optical studies of solid oxide fuel cells operating with dry and humidified oxygenated fuels. *ECS Trans.* **2011**, *35*, 2789–2798.
- (58) Pomfret, M.; Steinhurst, D.; Owrusky, J. Methanol and ethanol fuels in solid oxide fuel cells: A thermal imaging study of carbon deposition. *Energy Fuels* **2011**, *25*, 2633–2642.
- (59) Pomfret, M.; Marda, J.; Jackson, G.; Eichhorn, B.; Dean, A.; Walker, R. Hydrocarbon fuels in solid oxide fuel cells: in situ Raman studies of graphite formation and oxidation. *J. Phys. Chem. C* **2008**, *112*, 5232–5240.
- (60) Eigenbrodt, B.; Walker, R. In situ Raman measurements of solid oxide fuel cell devices. *Spectroscopy* **2014**, *29*, 24–30.
- (61) Larson, A.; Von Dreeles, R. GSAS. General Structure Analysis System. Los Alamos National Laboratory Report LAUR 86-748; The Regents of the University of California, 2000.
- (62) Segre, C.; Leyarovska, N.; Chapman, L.; Lavender, W.; Plag, P.; King, A.; Kropf, A.; Bunker, B.; Kemner, K.; Dutta, P.; Duran, R.; Kaduk, J. *CPS21, Synchrotron Radiation Instrumentation: Eleventh U.S. National Conference*; Pianetta, P., Ed.; American Institute of Physics: New York, 2000; pp 419–422.
- (63) Booth, C.; Bridges, F. Improved Self-Absorption Correction for Fluorescence Measurements of Extended X-Ray Absorption Fine-Structure. *Phys. Scr.* **2005**, *T115*, 202–204.
- (64) Ravel, B.; Newville, M. Athena, artemis, hephaestus: data analysis for X-ray absorption spectroscopy using IFEFFIT. *J. Synchrotron Radiat.* **2005**, *12*, 537–541.
- (65) Newville, M. IFEFFIT: interactive XAFS analysis and FEFF fitting. *J. Synchrotron Radiat.* **2001**, *8*, 322–324.
- (66) Lacheen, H.; Iglesia, E. Stability, structure and oxidation state of Mo/H-ZSM-5 catalysts during reactions of CH_4 and $\text{CH}_4\text{-CO}_2$ mixtures. *J. Catal.* **2005**, *230*, 173–185.
- (67) Berry, A.; O'Neill, H.; Jayasuriya, K.; Campbell, S.; Foran, G. XANES calibrations for the oxidation state of iron in a silicate glass. *Am. Mineral.* **2003**, *88*, 967–977.
- (68) Brownrigg, A.; Mountjoy, G.; Chadwick, A.; Alfredsson, M.; Bras, W.; Billaud, J.; Armstrong, A.; Bruce, P.; Dominko, R.; Kelder, E. In situ Fe K-edge X-ray absorption spectroscopy study during cycling of $\text{Li}_2\text{FeSiO}_4$ and $\text{Li}_{22}\text{Fe}_{0.9}\text{SiO}_4$ Li ion battery materials. *J. Mater. Chem. A* **2015**, *3*, 7314–7122.
- (69) Lassalle-Kaiser, B.; Merki, D.; Vrubel, H.; Gul, S.; Yachandra, V.; Hu, X.; Yano. Evidence from *in situ* A-ray absorption spectroscopy for the involvement of terminal disulfide in the reduction of Protons by an Amorphous Molybdenum Sulfide Electrocatalyst. *J. Am. Chem. Soc.* **2015**, *137*, 314–321.
- (70) George, S.; Drury, O.; Fu, J.; Friedrich, S.; Doonan, C.; George, G.; White, J.; Young, C.; Cramer, S. Molybdenum X-ray Absorption edges from 200–20,000 eV, the benefits of Soft X-ray Spectroscopy for Chemical Speciation. *J. Inorg. Biochem.* **2009**, *103*, 157–167.
- (71) Olimov, Kh.; Falk, M.; Buse, K.; Woike, Th.; Hormes, J.; Modrow, H. X-ray absorption near edge spectroscopy investigations of valency and lattice occupation site of Fe in highly iron-doped lithium niobate crystals. *J. Phys.: Condens. Matter* **2006**, *18*, 5135–5146.
- (72) Chankhantha, C.; Thanasuthipitak, P.; Kidkhunthod, P. Iron K-edge XANES study of heated green beryl from Madagascar. *Walailak J. Sci. Technol.* **2016**, *13*, 977–983.